CHEMISTRY OF MATERIALS

pubs.acs.org/cm

Article

Tuning Optical and Electrical Properties of Vanadium Oxide with Topochemical Reduction and Substitutional Tin

Lance M. Wheeler,* Thanh Luan Phan, Michelle A. Smeaton, Swagata Acharya, Shruti Hariyani, Marlena E. Alexander, Miranda I. Gonzalez, Elisa M. Miller, David W. Mulder, Sarbajit Banerjee, Katherine L. Jungjohann, Andrew J. Ferguson,* and Jeffrey L. Blackburn*

Cite This: *Chem. Mater.* 2024, 36, 10483−10495

Read Online

ACCESS | Metrics & More | Article Recommendations | Supporting Information

ABSTRACT: Vanadium oxides are widely tunable materials, with many thermodynamically stable phases suitable for applications spanning catalysis to neuromorphic computing. The stability of vanadium in a range of oxidation states enables mixed-valence polymorphs of kinetically accessible metastable materials. Low-temperature synthetic routes to, and the properties of, these metastable materials are poorly understood and may unlock new optoelectronic and magnetic functionalities for expanded applications. In this work, we demonstrate topochemical reduction of α-V_2O_5 to produce metastable vanadium oxide phases with tunable oxygen vacancies (>6%) and simultaneous substitutional tin incorporation (>3.5%). The chemistry is carried out at low temperature (65 °C) with solution-phase $SnCl_2$, where Sn^{2+} is oxidized to Sn^{4+} as V^{5+} sites are reduced to V^{4+} during oxygen vacancy formation. Despite high oxygen vacancy and tin concentrations, the transformations are topochemical in that the symmetry of the parent crystal remains intact, although the unit cell expands. Band structure calculations show that these vacancies contribute electrons to the lattice, whereas substitutional tin contributes holes, yielding a compensation doping effect and control over the electronic properties. The $SnCl_2$ redox chemistry is effective on both solution-processed V_2O_5 nanoparticle inks and mesoporous films cast from untreated inks, enabling versatile routes toward functional films with tunable optical and electronic properties. The electrical conductance rises concomitantly with the $SnCl_2$ concentration and treatment time, indicating a net increase in density of free electrons in the host lattice. This work provides a valuable demonstration of kinetic tailoring of electronic properties of vanadium−oxygen systems through top-down chemical manipulation from known thermodynamic phases.

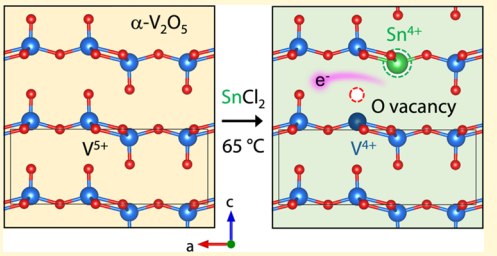

INTRODUCTION

The family of vanadium oxides receives immense interest due to its exceptional tunability of properties using stoichiometry,[1] crystal structure,[2] and doping.[3] Despite the rich history, the community continues to develop new insights into these materials, and they are considered a prototypical platform for applications related to the control and dynamic modulation of their optical and electronic properties. Various vanadium−oxygen stoichiometries have been explored for technologies ranging from optical modulators and electrochromic devices (i.e., dynamic windows) to nonlinear conductance switching (i.e., for memory, neuromorphic computing, or sensing).[4] Electrochemical energy storage is a particularly promising area, with a range of ion intercalation chemistries demonstrated.[5] Attractive features of vanadium oxides include the rich compositional space (phase diagram), associated variations of the crystal structure, a broad range of vanadium redox and spin states, and a correspondingly rich swath of electronic properties (spanning the range from insulator to semiconductor to metallic).[2,6]

The stability of many different oxidation states in vanadium oxides allows for many different polymorphs. Wadsley phases are a family of vanadium oxides, known to include V_2O_5, V_3O_7, V_4O_9, and V_6O_{13}, which correspond to a general formula: V_nO_{2n+1}, where $n = 2-6$.[4] The most oxidized compound V_2O_5 contains vanadium solely in the V^{5+} state. α-V_2O_5 is layered and is known to accommodate heterovalent atoms, either interstitially within the quasi-van der Waals gap or substitutionally at metal sites within the lattice. Interstitial cations from group 1 alkali metal (e.g., Li^+, Na^+, K^+) or group 2 alkaline earth metals (e.g., Mg^{2+}, Ca^{2+}) are routinely incorporated after synthesis using chemical or electrochemical methods.[4] Conversely, several transition metal (e.g., Ti^{4+}, Mn^{4+}, Mo^{6+}) and post-transition metal (e.g., Sn^{4+}, Al^{3+}, Bi^{3+}) ions have been incorporated as substitutional dopants into the α-V_2O_5 lattice.[7−16] Though examples of substitutional doping are prevalent, there are only a few reports of single-crystal or high-

Received: June 3, 2024
Revised: September 25, 2024
Accepted: September 30, 2024
Published: October 17, 2024

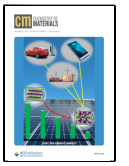

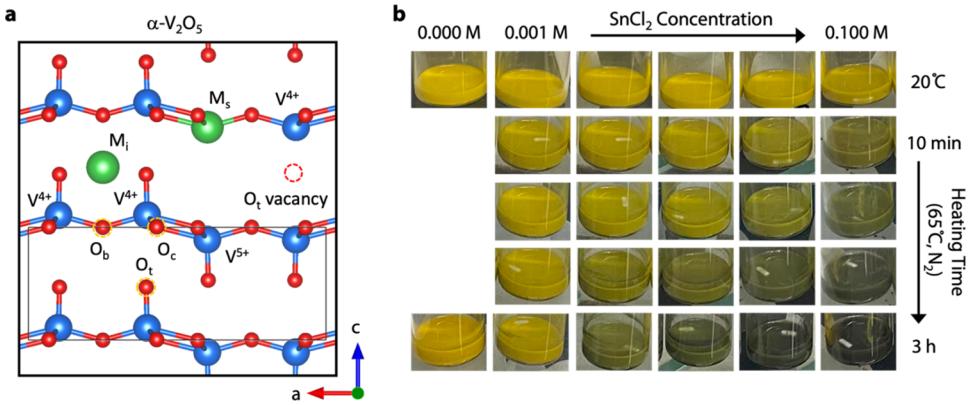

Figure 1. Chemical evolution of V_2O_5 from $SnCl_2$ redox chemistry. (a) Visualization of the lattice structure of α-V_2O_5 based on ICSD 60767. Thin black box highlights the α-V_2O_5 unit cell. O_t = terminal oxygen, O_b = bridging oxygen, and O_c = chain oxygen. M_s = substitutional metal heteroatom and M_i = interstitial metal heteroatom. (b) Photographs showing V_2O_5 dispersion color change as a function of $SnCl_2$ concentration and reaction time at 65 °C in an inert N_2 environment.

resolution structural data.[14,16] Thermodynamically stable phases of vanadium oxide are typically synthesized at high temperatures (>400 °C), and substitutional incorporation of heterovalent atoms is typically achieved during synthesis via sol−gel, hydrothermal/solvothermal, or solid-state synthetic routes at high temperature and/or pressures.[8,11−16] Examples of low-temperature post-synthesis methods for substitutional doping of the α-V_2O_5 structure have not been reported.

Vanadium can be reduced to form metastable oxygen vacancies within the vanadium oxide lattice. Vacancies are typically introduced using harsh chemical conditions like annealing at high temperatures in reducing (H_2) or inert environments.[17] There has been recent attention on topotactic (topochemical) transitions of vanadium oxide bronzes to achieve new polymorphs or altered ordering of interstitial sites in the binary vanadium oxide system.[2,18,19] Topotactic transitions are kinetically controlled structural phase changes accomplished by the ordered loss, gain, or rearrangement of atoms while maintaining the same crystallographic frameworks as the parent phase.[20] In addition to new binary phases of vanadium oxide, topochemical reduction reactions can also be leveraged to engender site-selective modification, modulate spin- and charge-ordering patterns, continuously expand the crystal lattice, avoid compensation reactions, and create nonequilibrium quantities of oxygen vacancies.[18,21,22] Topochemical reduction has been demonstrated in many transition metal oxide perovskite systems such as nickelates,[23−25] manganites,[26,27] ferrites,[28,29] and titanates[30,31] using a solid-state reaction with common reducing agents like CaH_2, LiH, and NaH, which yields oxygen vacancies in the host oxide lattice that are charge-balanced by protons.

In this work, we introduce the topochemical reduction and substitutional tin incorporation of α-V_2O_5 with solution-phase $SnCl_2$ at low temperatures (<65 °C). The low-temperature approach yields a metastable vanadium oxide material with oxygen vacancies and substitutional tin while maintaining the same crystal symmetry and average structure as those of the starting α-V_2O_5 material. The extents of vanadium reduction and tin doping are tunable using $SnCl_2$ concentration and reaction time, which yields control over the optical and electrical properties of vanadium oxide nanoparticles, both in solution and in mesoporous V_2O_5 nanoparticle films. As we increase the concentration of $SnCl_2$ (0−0.10 M) or extend the treatment duration (0 to 90 min), we observe a corresponding rise in the concentration of oxygen vacancies and concomitant V^{4+} and Sn^{4+} in the lattice. All-electron quasiparticle self-consistent (QS) GW method calculations confirm that vacancies contribute free electrons to the lattice, whereas Sn^{4+} contributes holes. The tunable chemistry maps to a correspondingly tunable density of free electrons and electrical conductance in mesoporous α-V_2O_5 thin films, which we track with both contactless (9 GHz) and two-terminal device conductance measurements. This study presents a significant demonstration of tailoring the vanadium−oxygen system through top-down chemical manipulation. Such advancements hold promise for next-generation optoelectronic applications.

RESULTS AND DISCUSSION

Low-Temperature $SnCl_2$ Chemistry. α-V_2O_5 is thermodynamically favored to crystallize into the orthorhombic (*Pmmn* symmetry) structure composed of VO_5 pyramids (Figure 1a).[32] Oxygen atoms exist in three distinct bonding states: Chain oxygens (O_c) are bonded to two V^{5+} atoms, bridging oxygen (O_b) is bonded to three V^{5+} atoms, and the terminal vanadyl oxygen (O_t) is bonded to a single V^{5+} atom and protrudes into the quasi-van der Waals (vdW) gap. Compared to the double and triple coordination of chain and bridging oxygens, respectively, the terminal oxygen has the lowest energy reaction pathway to form vacancies that are known to modulate the V_2O_5 Fermi level and conductivity.[33] Metal heteroatoms can incorporate into the V_2O_5 lattice substitutionally (M_s) for high valency metals (≥3+) or interstitially (M_i) for lower valency (<3+).[34] Interstitial heteroatoms typically sit in the quasi-van der Waals gap but alternative sites have been demonstrated.[35] Interstitial sites can be readily accessed through shear distortions that alter the stacking sequences of infinite V_2O_5 sheets.[2,3]

The addition of $SnCl_2$ to suspensions of V_2O_5 nanoparticles at concentrations ranging from 1 to 100 mM produced visual (and tunable) color change, even at room temperature. The reaction proceeded more rapidly at 65 °C to produce colors evolving from yellow to army green to near black over the course of 3 h (Figure 1b). Treating metal oxides with a solution of $SnCl_2$ has been shown to significantly affect the optical and electrical behavior through a presumed intercalation reaction.[36,37] Since $SnCl_2$ is known to disproportionate ($2Sn^{2+}Cl_2 \rightarrow Sn^0 + Sn^{4+}Cl_4$) in the presence of acetone and tartaric acid,[37,38] several publications have proposed that zerovalent Sn^0 intercalates into the van der Waals gap of metal oxides and other layered

https://doi.org/10.1021/acs.chemmater.4c01557
Chem. Mater. 2024, 36, 10483−10495

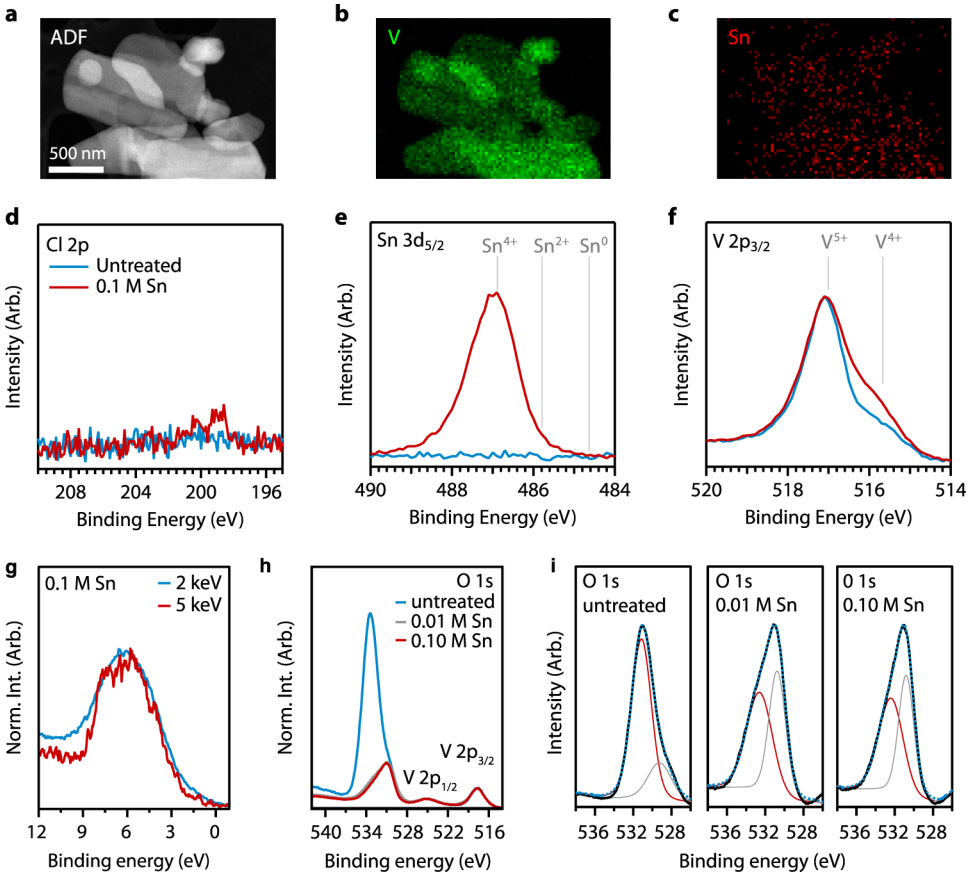

Figure 2. Composition of $SnCl_2$-treated V_2O_5. (a) Annular dark-field (ADF) STEM image of $SnCl_2$-treated V_2O_5. (b, c) Energy-dispersive X-ray map of vanadium (b) and tin (c) over the same area as the ADF image. (d–f) XPS core-level spectra of V_2O_5 and 0.1 M $SnCl_2$-treated V_2O_5 highlighting the (d) Cl 2p, (e) Sn $3d_{5/2}$, and (f) V $2p_{3/2}$ regions. (g) Energy-variant valence band HAXPES spectra of 0.10 M $SnCl_2$-treated V_2O_5 are closely overlapped at 2 and 5 keV excitation, which suggests the absence of $5s^2$ stereochemically active lone pairs characteristic of divalent tin. This confirms the nominally tetravalent oxidation state assignment of the incorporated Sn. (h) V 2p and O 1s core-level HAXPES spectra acquired at 2 keV normalized to V $2p_{3/2}$ depict a clear decrease in the relative O 1s intensity of the $SnCl_2$-treated compounds, which is attributed to the formation of oxygen vacancies. (i) Change in the O 1s peak shape and fits illustrate the evolution of the oxygen local environment because of the oxygen vacancies and tin incorporation. The dashed blue line is a composite fit.

chalcogenide hosts due to reaction with solutions of $SnCl_2$.[39] However, we observe the same color change with and without tartaric acid in a variety of solvents (Methods), suggesting this Sn^0 mechanism is unlikely.

Vanadium Reduction and Tin Doping. Redox chemistry is a more likely result than Sn^0 intercalation when $SnCl_2$ solutions are combined with V_2O_5 nanoparticles. $SnCl_2$ is known to be a strong reducing agent, and V_2O_5 is conversely a strong oxidizing agent, which is used industrially in the contact process to produce sulfuric acid. It has also been shown to undergo phase transitions, e.g., to VO_2, under cathodic bias by losing oxygen.[40] The standard redox potential of the Sn^{2+}/Sn^{4+} couple is +0.15 V, while that of the V^{4+}/V^{5+} couple is +1.0 V (both vs NHE), providing a ca. 0.85 V driving force for the redox reaction in which electrons are transferred from $SnCl_2$ to the α-V_2O_5 lattice, oxidizing Sn^{2+} to Sn^{4+}. The electrons liberated from Sn^{2+} should thus reduce V^{5+} to V^{4+}, which must be balanced by the loss of an O atom from the α-V_2O_5 lattice. Sn^{4+} has also been shown to act as a substitutional dopant in α-V_2O_5.[8]

Based on the above considerations, we propose the following redox reaction that accommodates the possibility of Sn substitution:

$$x\mathrm{Sn}^{2+}\mathrm{Cl}_2 + \mathrm{V}_2^{5+}\mathrm{O}_5 \rightarrow (x - 2xy)\mathrm{Sn}^{4+}\mathrm{OCl}_2 + 2xy\mathrm{V}^{4+}\mathrm{OCl}_2 + (\mathrm{Sn}_y^{4+}\mathrm{V}_{1-y}^{4+})_{2x}\mathrm{V}_{2-2x}^{5+}\mathrm{O}_{5-x} \quad (1)$$

where x is the fraction of oxygen vacancies and y is the fraction of Sn^{4+} that exchanges with V^{4+} lattice sites in the mixed-valence vanadium oxide. As the reaction proceeds, the ratio of V^{4+} and Sn^{4+} to V^{5+} increases in vanadium oxide. To remove one oxygen atom to form a vacancy, two vanadium atoms must be reduced or a vanadium atom must be replaced by Sn^{4+}. In this scheme, oxygen atoms are abstracted from the V_2O_5 lattice to form the solvated $SnOCl_2$ or $VOCl_2$. Many solvates of $VOCl_2$ are known,[41] and $SnCl_2$ is known to be oxidized by molecular oxygen and should readily react with an oxygen radical abstracted from the V_2O_5 lattice.[42] Messin and Janier-Dubry showed that the reaction product was tin oxychloride rather than SnO_2 and Cl_2,[43] and the reaction only proceeded in coordinating solvents, including tetrahydrofuran, pyridine, and acetonitrile. If $y = 0$ and the reaction occurs to yield thermodynamically stable crystal structures, each of the known Wadsley phases of mixed-valence vanadium oxides are possible as x is increased: V_3O_7 at $x = 1/3$, V_4O_9 at $x = 1/2$, V_6O_{13} at $x = 2/3$, and VO_2 at $x = 1$. Density functional theory (DFT) studies have predicted midgap

https://doi.org/10.1021/acs.chemmater.4c01557
Chem. Mater. 2024, 36, 10483−10495

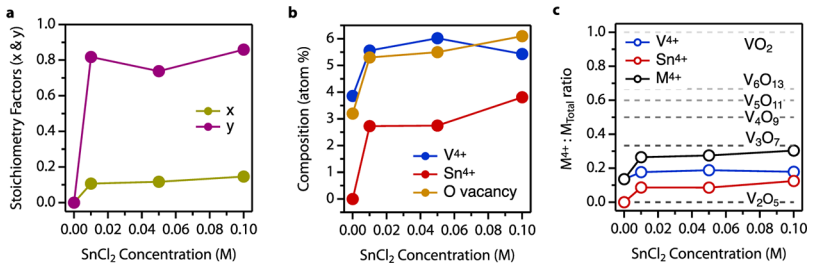

Figure 3. (a) Evolution of x (oxygen vacancies) and y (Sn^{4+} substitution) from eq 1 as a function of $SnCl_2$ concentration for a 90 min reaction as determined from XPS (Methods). (b, c) Composition of V^{4+} and Sn^{4+} (b) and ratio of M^{4+} to total metals in the sample (c) as a function of $SnCl_2$ concentration for a 90 min reaction as determined from XPS. Dashed lines correspond to expected M^{4+}:M_{Total} ratio for known thermodynamically stable vanadium oxide compounds.

states due to both oxygen vacancies (change in x)[44,45] and tin incorporation (change in y),[46] which is consistent with our observation in the change in color of V_2O_5.

We confirm that Sn is incorporated into the vanadium oxide nanoparticles through energy-dispersive X-ray spectroscopy (EDX) and X-ray photoelectron spectroscopy (XPS) analyses, including hard X-ray photoemission spectroscopy (HAXPES) probing tens of nanometers into the bulk (Figure 2). Annular dark-field (ADF) scanning transmission electron microscopy (STEM) images show that the $SnCl_2$-treated α-V_2O_5 nanoparticles are polydisperse with nonspherical shapes and typical dimensions between 100 and 500 nm (Figure 2a). EDX maps of the same V_2O_5 nanoparticles show that V (Figure 2b) and Sn (Figure 2c) are uniformly distributed in the V_2O_5 nanoparticles and point to the absence of Sn or Sn-rich phases segregated to the nanoparticle surface. XPS allows us to confirm that the Sn detected in EDX is not due to residual $SnCl_2$ precursor, as the Cl 2p signal is negligible (Figure 2d) compared to the strong signal exhibited by the Sn $3d_{5/2}$ peak (Figure 2e). We employed a thorough washing procedure of repeated centrifugation and dispersion in methanol that effectively removes all Cl byproducts (Methods).

XPS reveals the presence of surface (top ~10 nm) Sn and oxygen vacancies in the vanadium oxide lattice. The oxidation state of tin in the vanadium oxide samples is Sn^{4+} rather than Sn^{2+} or Sn^0, which is consistent with eq 1 (Figure 2e). Based on SnO_2/SnO studies, Sn^{4+} exists in an octahedral bonding environment with six oxygens and is expected to have a 0.7 eV higher binding energy (ca. 486.4 eV) than Sn^{2+} (ca. 485.7).[47] Sn^0 is expected at even lower binding energies (ca. 484.5 eV).[48] V^{4+} (ca. 516 eV) and V^{5+} (ca. 517 eV) have an electron binding energy difference of roughly 1 eV (Figure 2f).[49,50] The presence of V^{4+} is an indication of oxygen vacancies, as two V^{5+} atoms must be reduced to V^{4+} or replaced by Sn^{4+} to form a single oxygen vacancy (eq 1).

As topochemical reactions can yield transformations confined to the surface, HAXPES was utilized to probe Sn substitution and O vacancy formation within the bulk material. The higher incident energies of high-resolution synchrotron HAXPES yield increased penetration depths (~10−30 nm) compared to laboratory XPS sources.[51] HAXPES core-level spectra were first measured at an excitation energy of 2 keV, exhibiting features centered at ca. 496.6 eV and ca. 488.2 eV. These correspond to Sn^{4+} $3d_{3/2}$ and $3d_{5/2}$, which suggests that the Sn^{4+} substitution extends further into the bulk from the surface than can be probed with laboratory XPS (Figure S1). The intensities of the Sn^{4+} $3d_{3/2}$ and $3d_{5/2}$ peaks also increase upon treatment of V_2O_5 with higher concentrations of $SnCl_2$, suggesting increased substitution of Sn^{4+}. Core-level HAXPES was also unable to detect Cl within the bulk of the material (Figure S2).

The Sn oxidation state was further confirmed as nominally tetravalent by measuring the valence band using energy-variant HAXPES. Sn^{2+} manifests the stereochemical activity of its $5s^2$ electron lone pairs upon appropriate anion hybridization, whereas Sn^{4+} does not.[52] The presence of stereochemically active lone pairs can be directly observed through energy-variant HAXPES since the photoionization cross section of the filled 5s/6s orbitals of p-block cations do not decay as sharply at high incident photon energies.[19] Therefore, the valence band HAXPES spectra collected at higher incident energies would more prominently feature orbital contributions from the Sn^{2+} lone pair of electrons. Previous literature has shown that a distinct feature in the energy-variant valence band HAXPES spectrum of β-$Sn_{0.33}V_2O_5$ arises at ca. 11 eV and increases in intensity upon increasing photon energy, indicative of the stereochemical activity of the Sn^{2+} lone pair of electrons.[53] However, the energy-variant valence band HAXPES spectra of 0.10 M $SnCl_2$-treated V_2O_5 collected at 2 and 5 keV are virtually identical in terms of shape and intensity (Figure 2g). This result can only be obtained if the Sn atoms do not contain stereochemically active lone pairs, which further supports the assignment of the Sn^{4+} oxidation state.

Normalizing the O 1s and V 2p HAXPES spectra to the V $2p_{3/2}$ signal clearly depicts a decrease in the O 1s signal upon treatment with $SnCl_2$, arising from the presence of oxygen vacancies (Figure 2h). Furthermore, fitting the O 1s peak of the HAXPES spectra allows for the local coordination of the oxygen atoms to be probed in extensive detail. The local oxygen coordination environment clearly evolves upon Sn^{4+} substitution and the formation of lattice oxygen vacancies, as evidenced by the drastic change in the O 1s peak shape (Figure 2i).

Varying the $SnCl_2$ concentration allows us to systematically tune the concentration of oxygen vacancies and Sn substitution in the vanadium oxide host. For 90 min reactions employing $SnCl_2$ concentrations from 0.0 to 0.1 M $SnCl_2$, oxygen vacancy concentration (x) monotonically increases, from 0.10 to 0.15 with increasing $SnCl_2$ concentration, based on XPS (Figure 3a). In the same reaction series, the ratio of Sn^{4+} to V^{4+} (y, eq 1) increases from 0 to ~0.8 and remains relatively constant with increasing $SnCl_2$. The data suggest that Sn substitution favors the formation of V^{4+}. We also present the data in absolute atomic percent (Figure 3b). There is a ~4 atom % population of V^{4+} in the untreated α-V_2O_5, which increases to >6 atom % after treatment with 0.1 M $SnCl_2$. Sn^{4+} monotonically increases up to >3.5 atom % after exposure to 0.1 M $SnCl_2$ for 90 min. The result of V^{4+} formation and Sn^{4+} incorporation leads to a significant

https://doi.org/10.1021/acs.chemmater.4c01557
Chem. Mater. 2024, 36, 10483−10495

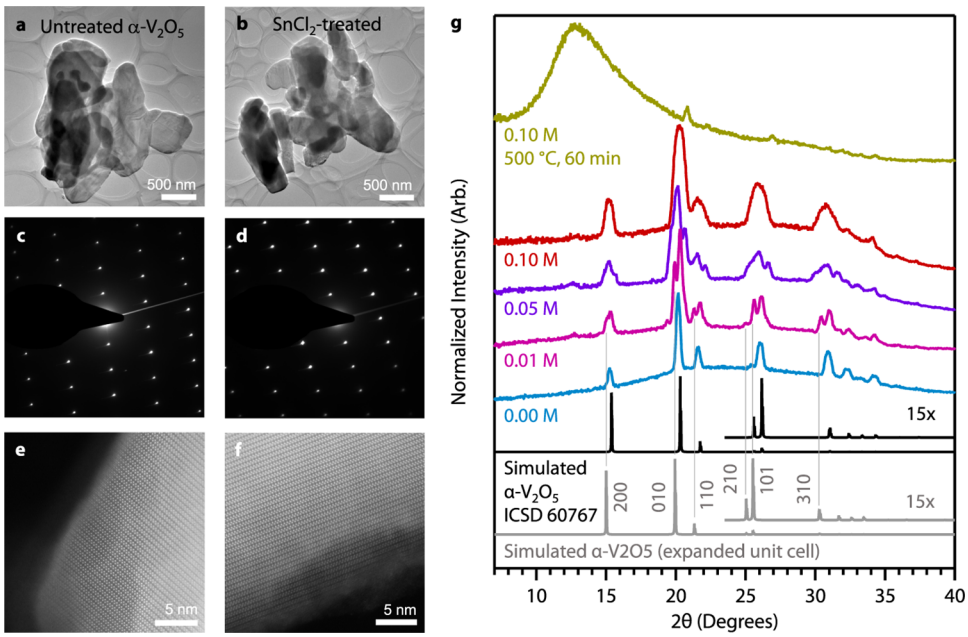

Figure 4. Structural evolution of V_2O_5 from $SnCl_2$ redox chemistry. (a, b) Transmission electron microscopic (TEM) images of untreated α-V_2O_5 (a) and 0.05 M $SnCl_2$-treated V_2O_5 (b). (c, d) Selected-area diffraction images of untreated α-V_2O_5 (c) and 0.05 M $SnCl_2$-treated V_2O_5 (d). (e, f) Annular dark-field scanning transmission electron microscopic (ADF-STEM) images of untreated α-V_2O_5 (e) and 0.05 M $SnCl_2$-treated V_2O_5 (f). (g) Powder X-ray diffraction patterns of untreated α-V_2O_5 (0.00 M) and V_2O_5 samples with increasing $SnCl_2$ concentration. The 2θ axis is relative to Cu Kα (1.5406 Å, 8.04 eV) radiation. The α-V_2O_5 pattern was simulated and expanded using VESTA software from ICSD 60767.

loss in oxygen in the lattice, with oxygen vacancies reaching ~6% after treating the sample with 0.1 M $SnCl_2$ for 90 min (Figure 3b).

Topochemical Transformation. In prior work, restructuring was not observed in nanoparticles with up to 5% oxygen vacancy concentration.[33] Here, we show a vacancy concentration of up to ~6% based on XPS tin and vanadium peaks; HAXPES results indicate that oxygen vacancy formation is not just on the surface but extends at least 30 nm into the bulk. The relative concentration of 4+ metal atoms ($M^{4+} = Sn^{4+} + V^{4+}$) to the total number of atoms in the lattice approaches the concentration expected for V_3O_7 (Figure 3c). We thus expect additional phases of vanadium oxide to appear. High-temperature reduction of stoichiometric α-V_2O_5 typically proceeds through multiple simultaneous Wadsley-phase intermediates and ends with V_2O_3, a Magnéli phase.[17] High-temperature reduction produces thermodynamically stable intermediate crystal structures, which are accessed through a series of relatively low-energy crystallographic shear transformations along different directions that eliminate ordered arrays of oxygen vacancies, whereas our topochemical approach yields a crystal structure that preserves long-range ordering.

Transmission electron microscopic (TEM) images show that untreated α-V_2O_5 nanoparticles are polydisperse and remain unchanged after treatment with $SnCl_2$ (Figure 4a,b). Selected-area diffraction patterns (Figure 4c,d) show that the transformations induced by $SnCl_2$ were topotactic in nature, despite the large changes in stoichiometry. The materials maintain their crystallinity with similar electron diffraction patterns, which suggests that the overall framework is preserved. ADF-STEM images of the edge of V_2O_5 nanoparticles before and after $SnCl_2$ treatment show lattice fringes extending to within ~1 nm of the particle surface with minimal changes in lattice spacing (Figure 4e,f). Noncrystalline material at the surface may be amorphous vanadium oxide or simply adventitious carbon.

X-ray diffraction (XRD) confirmed that the vanadium oxide samples maintain their crystal symmetry after topochemical reduction and tin incorporation. Untreated α-V_2O_5 exhibited the expected orthorhombic reflections indicative of *Pmmn* (No. 59) symmetry (Figure 4g).[54] After $SnCl_2$ treatment, new reflections emerged that we attribute to an expansion of the unit cell (Figure 4d), but not the appearance of new crystalline phases, oxychlorides, or tin oxides. Previous studies on substitutional tin doping report inconsistent lattice parameters based on powder X-ray diffraction, with all works reporting expansion of the *a*-axis and either expansion or contraction of the *b* and *c* axes.[7−10] Studies on the analogous α-MoO_3 system also showed that increasing oxygen vacancy content led to an increase in unit cell dimensions.[55] A 90 min treatment with 0.01 M $SnCl_2$ yields a significantly expanded α-V_2O_5 unit cell with shifts to lower angles for the prominent 010, 110, 210, and 310 reflections.

The evolution of the XRD patterns resembles reports of hydrogen intercalation into α-V_2O_5 where reflections shift, split, and evolve with increasing hydrogen concentration but without signs of additional phases.[56] At 0.1 M $SnCl_2$, the distinct reflections merge into broad peaks, indicating short-range disorder but a crystal that has still maintained a long-range order. Raman spectroscopy on the same samples also indicated no new phases and maintained bonding motifs within the lattice (Figure S5). We did not observe multiple peaks for each reflection using electron diffraction (Figure 4d), but the pattern contracted after treatment, which is consistent with the expanded lattice observed in XRD (Figure S4). Since powder X-ray diffraction is volume-weighted over a large area compared to electron diffraction of individual particles in the electron microscope, we hypothesize that the appearance of multiple peaks at each reflection in XRD is due to a sampling of multiple nanoparticle populations where smaller particles react faster

https://doi.org/10.1021/acs.chemmater.4c01557
Chem. Mater. 2024, 36, 10483−10495

Table 1. Characteristics of V_2O_5 Compounds Exhibiting Orthorhombic *Pmmn* Space Group Symmetry Broken Down into Three Types of Heteroatom Incorporation[a]

	Host crystal	Interstitial (vdW gap)			interstitial (O_b plane)		Substitutional	
	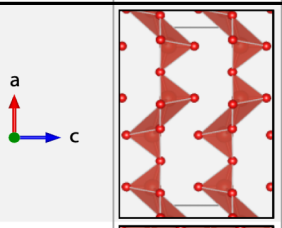							
	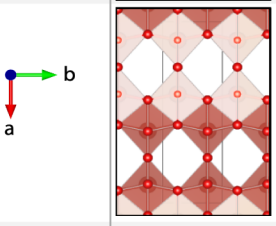							
Stochiometry	α-V_2O_5	LiV_2O_5	NaV_2O_5	CaV_2O_5	$Fe_{0.11}V_2O_{5.16}$	$Cr_{0.11}V_2O_{5.16}$	$(Mo_{0.1}V_{0.9})_2O_5$	This work
a	11.512	11.552	11.311	11.351	11.540	11.485	11.560	11.800
Δa (%)	-	0.347	-1.746	-1.399	0.243	-0.235	0.417	2.502
b	4.368	4.655	4.800	4.893	4.350	4.382	4.333	4.450
Δb (%)	-	6.566	9.890	12.019	-0.412	0.314	-0.797	1.877
c	3.564	3.573	3.610	3.604	3.563	3.564	3.577	3.650
Δc (%)	-	0.258	1.291	1.122	-0.031	-0.014	0.351	2.413
Heteroatom valency	V^{4+}	Li^+	Na^+	Ca^{2+}	Fe^{3+}	Cr^{3+}	Mo^{6+}	Sn^{4+}
Heteroatom crystal radius (Å) (CN = 6)*	0.72	0.9	1.16	1.13	0.69 (LS) 0.79 (HS)	0.76	0.73	0.83 (Sn^{4+})
ICSD	60767	88639	59345	82689	86179	86180	99813	

[a]Large red atoms = vanadium, small red atoms = oxygen, yellow atoms = sodium, and blue octahedra = $[CrO_6]^{9-}$. Crystal structure characteristics are based on ICSD entries from various literature sources.[14,32,58−61] vdW = van der Waals. *Crystal radii are based on Shannon,[62] with the exception of Sn^{2+}, which is based on Sidey et al.[63] LS = low spin, HS = high spin, CN = coordination number.

than larger ones. We observe a similar XRD pattern evolution when using acetone as the solvent (Figure S6).

Samples that were treated with 0.1 M $SnCl_2$ and subsequently annealed in air at 500 °C became mostly amorphous, indicating that the high oxygen vacancy concentration and substitutional Sn achieved here are only kinetically accessible through low-temperature topochemistry (Figure 4g). The preservation of the average structure with a layered orthorhombic leitmotif, evidenced in lattice-resolved TEM imaging, electron diffraction, and powder X-ray diffraction, indicates that crystallographic shear transformation is considerably impeded. Shear transformations are characteristic of binary vanadium oxides and drive structural transformations through a sequence of phases. We posit that substitutional Sn atoms positioned on the vanadium sublattice can prevent vacancy reordering and crystallographic shear transformations in a manner reminiscent of dopants freezing motion of dislocations through periodic lattices.[57]

Topochemical transformations are known to occur in α-V_2O_5, but exchange at the vanadium site for other cations has only been shown for bottom-up synthesis. We compiled known V_2O_5-derived materials with heteroatoms incorporated into the structure that maintain the *Pmmn* space group symmetry and compared them to the V_2O_5 sample treated with 0.01 M $SnCl_2$ (Table 1). Materials are grouped by the location of the heteroatoms. The most heavily studied subset of these materials is for battery cathode applications and can be produced topochemically or electrochemically by intercalation of alkali or alkaline earth metals (e.g., LiV_2O_5,[58] NaV_2O_5,[59] and CaV_2O_5[60]). In these materials, the intercalated ion has a valency ≤2 and a large crystal radius of ≥0.9 Å.[62] The atoms insert interstitially into the vdW gap where they are charge-balanced by reduced vanadium sites (V^{4+}) that maintain their 5-fold oxygen coordination. vdW gap insertion leads to a large change in the *b*-axis of the unit cell compared to the parent compound (Δb > 6%). The relative amount of Sn^{4+} to V^{4+} based on XPS and HAXPES makes interstitial incorporation of Sn^{4+} into V_2O_5 unlikely. Four V^{4+} atoms are needed to balance a single interstitial Sn^{4+} atom. XPS shows that the V^{4+}-to-Sn^{4+} ratio is closer to 2 (Figure 3b).

Higher valency ions such as Cr^{3+} and Fe^{3+} have smaller crystal radii and have been shown to insert interstitially close to the plane made by the bridging oxygens rather than within the vdW gap. Oxygen atoms also accompany the interstitial cations to increase the overall V:O ratio, in contrast to what we observe here. $Cr_{0.11}V_2O_{5.16}$ and $Fe_{0.11}V_2O_{5.16}$ have been synthesized from a bottom-up sol-gel process, but there are no reports of topochemical access of these compounds.[61]

https://doi.org/10.1021/acs.chemmater.4c01557
Chem. Mater. 2024, 36, 10483−10495

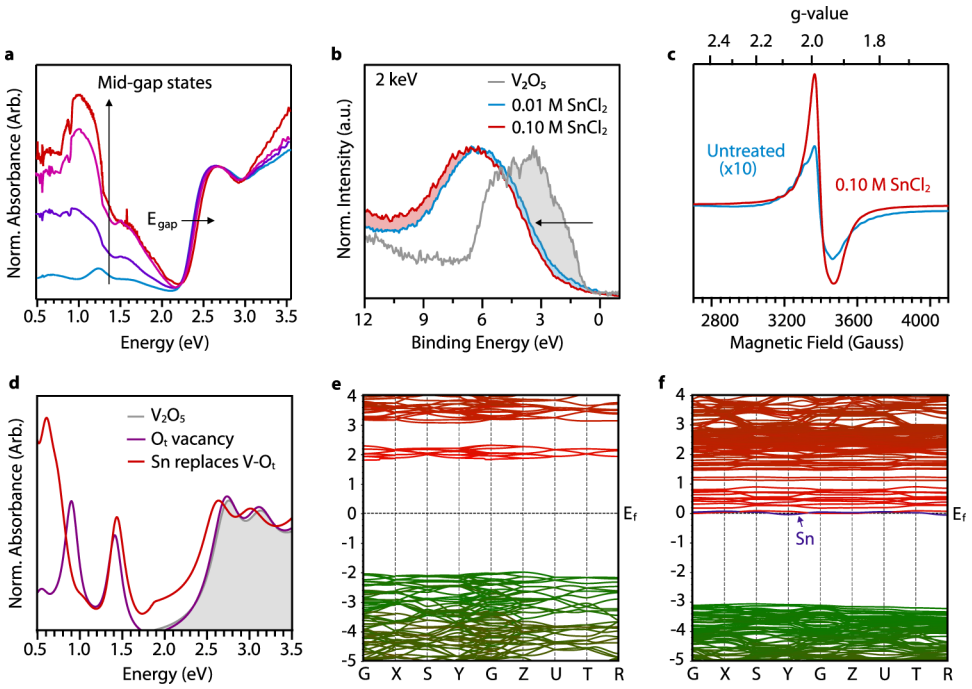

Figure 5. Optical and electrical properties of $SnCl_2$-treated V_2O_5 nanoparticles. (a) UV−vis−NIR absorbance of α-V_2O_5 films as a function of $SnCl_2$ treatment. Spectra are normalized at 2.75 eV and offset to account for scattering. (b) Valence band HAXPES spectra of α-V_2O_5 and 0.01 and 0.10 M $SnCl_2$-treated α-V_2O_5 measured at 2 keV show a clear increase in the energy separation between the Fermi level and the valence band edge, consistent with the Moss−Burstein effect arising from a population of conduction band electrons that are thermally excited from midgap vacancy states. (c) Electron paramagnetic resonance (EPR) spectra of untreated α-V_2O_5 and 0.1 M $SnCl_2$-treated α-V_2O_5 collected at 60 K. (d) Absorbance spectra from theoretical calculations based on a quasiparticle self-consistent GW (QSGW) approximation, illustrating midgap absorption bands due to oxygen vacancies and Sn substitution. (e, f) Electronic band structures for undoped (stoichiometric) α-V_2O_5 (e) and Sn substitution for V = O_t into the α-V_2O_5 lattice (f).

The radius of Sn^{4+} (0.83 Å) in 6-fold coordination is larger than that of V^{4+} (0.72 Å), but not as large as ions known to intercalate into the vdW gap. DFT shows that high valency metals (>3+) such as Sn^{4+} are more thermodynamically favored as substitutional rather than interstitial dopants.[34] Though Sn^{4+}, Ti^{4+}, and Bi^{3+} have been reported as substitutional dopants in the V_2O_5 lattice,[8,11,12] only Mo^{6+}-doped V_2O_5 had a single-crystal or high-resolution structure data available.[14,16] Mo^{6+} has nearly the same crystal radius as V^{5+}, whereas Sn^{4+} is ∼13% larger, which leads to larger structural distortions in each direction of the unit cell. Delocalization of electron density between Mo and V sites was observed in Mo and V K-edge XANES analyses of substitutionally doped V_2O_5 indicating a formal Mo valence between +5 and +6.[16] Notably, substitutional Mo doping considerably expands phase stability regimes by introducing local distortions, such as increased puckering of the V_2O_5 layers and canting of the vanadyl oxygens. The suppression of crystallographic shear transformations in the Sn-doped V_2O_5 presented here appears to be directly analogous to the suppression of the intercalation-driven layer shearing in Mo-alloyed V_2O_5.[16,64]

Optical and Electrical Properties. The topochemical approach shown here is unique in the V_2O_5 literature in installing a p-block cation directly on the vanadium sublattice and demonstrates a new avenue to tailor the properties of the material. Material structure and composition are intimately linked to optical and electronic properties. UV−vis absorption spectroscopy shows that treatment with increasing $SnCl_2$ concentration induces a systematic hypsochromic (blue) shift of the primary absorption onset at ca. 2.2 eV, along with the growth of a broad envelope of lower energy optical transitions below 2.2 eV (Figure 5a).

These observations are consistent with the introduction of oxygen vacancies and conduction band electrons. According to previous DFT calculations, we expect oxygen vacancies to give rise to midgap states with energies ranging from ca. 0.69 to 0.95 eV above the valence band maximum. Peaks arise due to corresponding oxygen vacancies in terminal, bridging, and chain coordination geometries/environments.[45] These states are present even before $SnCl_2$ treatment, which is consistent with the observation of V^{4+} in XPS spectra of untreated V_2O_5 (Figure 2f). Since these vacancy sites are occupied with electrons,[45] they give rise to the observed optical transitions that correspond to promotion of these localized electrons to the conduction band, where the sub-band gap peak intensities are proportional to the vacancy density.

The density of occupied vacancy sites is also expected to move the Fermi level (E_F) closer to (or into) the conduction band due to thermal excitation of electrons to the conduction band. The systematic blue shift of the ca. 2.2 eV band gap absorption onset with increasing $SnCl_2$ is consistent with the Moss−Burstein shift arising from a progressively increasing E_F, consistent with that observed previously for lithium-modulated vacancy formation in V_2O_5.[44] The position of E_F was probed with HAXPES, and the valence band of untreated V_2O_5 measured at 2 keV is shown in Figure 5b and compared with similar data for 0.01 and 0.10 M $SnCl_2$-treated V_2O_5. The distance between the valence band edge and E_F increases upon $SnCl_2$ treatment, consistent with the Moss−Burstein shift and the notion that oxygen vacancies contribute electron density to the V_2O_5 conduction band. The valence bands measured at 5 keV, which probe up to 30 nm

https://doi.org/10.1021/acs.chemmater.4c01557
Chem. Mater. 2024, 36, 10483−10495

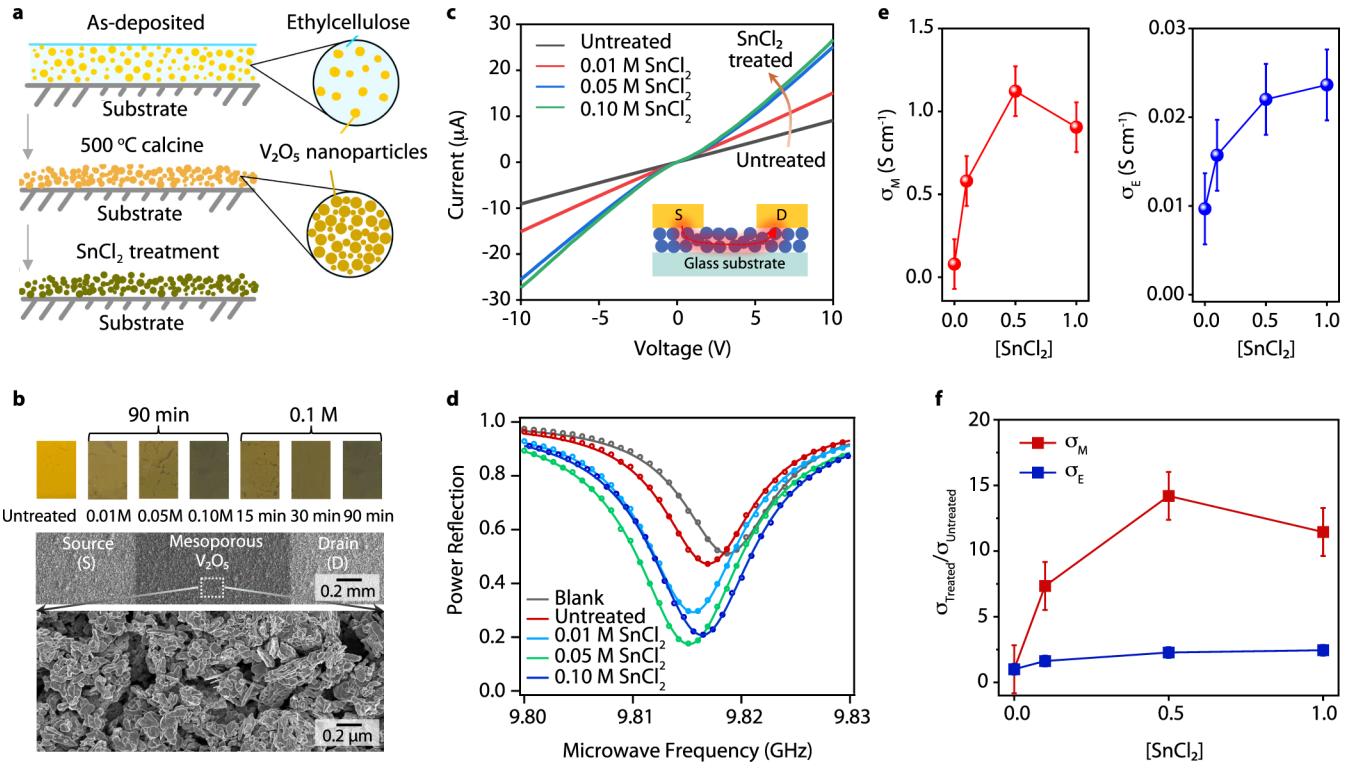

Figure 6. Optical and electrical characterization of the $SnCl_2$-treated V_2O_5 film. (a) Cartoon illustrating preparation and treatment of mesoporous α-V_2O_5 films. (b) Photographs of mesoporous films treated with increasing concentration of $SnCl_2$ for 90 min and evolution of a treatment with 0.1 M $SnCl_2$ as a function of time (top panel). The bottom panel presents a scanning electron microscopic (SEM) image of the Au/α-V_2O_5/Au device, highlighting the source/drain contact on the mesoporous α-V_2O_5 film, and a zoomed-in view of the mesoporous α-V_2O_5 structure within the channel. (c) Current−voltage characteristics of the Au/α-V_2O_5/Au device corresponding to various concentrations of $SnCl_2$ treatment: 0.01, 0.05, and 0.10 M, each treated for 90 min. The inset shows a schematic side view of the device, illustrating the current flow between the source and drain contacts through the mesoporous α-V_2O_5 film. (d) Microwave conductivity power reflection resonance curves for untreated and $SnCl_2$-treated films at various concentrations (0.01, 0.05, and 0.10 M). Circles represent the experimental data, while lines indicate the fitted data. The blank refers to the quartz substrate prior to the deposition of the mesoporous α-V_2O_5 film. (e) Conductivity values extracted from noncontact microwave conductivity and two-terminal device electrical measurements for the film treated with different concentrations of $SnCl_2$. (f) Comparison of the conductivity ratio between untreated and $SnCl_2$-treated sample, as measured by noncontact microwave conductivity and for two-terminal devices.

within the bulk material due to the higher incident photon energy, also show a similar trend (Figure S3).

The new sub-band gap states observed in optical absorption from formation of oxygen vacancies in the host lattice led to an increased number of free electrons and V^{4+} (eq 1). Electron paramagnetic resonance (EPR) is sensitive to unpaired electrons and has also been shown to be a useful tool for identifying V^{4+} in vanadium oxides.[65] The weak EPR signal at g-value ∼2 for the untreated α-V_2O_5 that is a superimposed hyperfine structure that indicates coupling of the electron spins to V^{4+} nuclei (Figure 5d). This is consistent with electron doping due to adventitious oxygen vacancies.[66] Treatment with 0.1 M $SnCl_2$ induces a resonance feature that is >10× more intense than the untreated sample, indicating a significant increase in the concentration of free electrons and V^{4+} (Figure 2e). Sn^{4+} and Sn^{2+} centers are not EPR-active and will not contribute to the observed EPR signal.

We verify our experimental findings with theoretical calculations based on quasiparticle self-consistent GW (QSGW) approximation[67] using the primitive cell of bulk α-V_2O_5, which contains 14 atoms. We have reported the electronic properties and optical spectra of bulk α-V_2O_5 in our previous work and show the optical spectrum in Figure 5d, where a thorough analysis indicates that the features located at energies above ca. 2.2 eV are purely excitonic in nature.[68] To simulate the effects of oxygen vacancies and substitutional Sn^{4+} on the electronic structure and optical properties, we constructed an 84-atom supercell. GW is a theory for many-body scattering, and the optical spectra are computed with the full dynamical self-energy, i.e., considering both the electronic eigenvalues and their lifetime effects via the imaginary part of the dynamical self-energy. This allows simulation of several broad midgap (0.5−2.0 eV) optical absorptions when oxygen vacancies and Sn^{4+} are introduced into the lattice (Figure 5d), consistent with measured optical spectra (Figure 5a).

Band structure calculations that complement optical absorptions show a 3.8 eV band gap (and 2.2 eV optical gap) and Fermi level (E_F) in the middle of the band gap, as expected for undoped V_2O_5 (Figure 5e). Simulations reveal that formation of a vanadyl oxygen (O_t) vacancy adds two electrons, raising the Fermi level to the conduction band minimum. Conversely, it is pushed into the valence hole-like states when Sn^{4+} dopes the system. When one Sn^{4+} atom replaces a V−O_t unit, it compensates for the oxygen vacancy and the system effectively gains one net electron. The overall electronic structure is metallic with the partially filled V (red) and Sn (blue) states crossing the Fermi level (Figure 5f).

Thin Film Chemistry and Devices. We demonstrate that topochemical $SnCl_2$ reduction chemistry is also possible in mesoporous thin films of α-V_2O_5 fabricated by formulating a viscous ethylcellulose-based ink that may be processed to

https://doi.org/10.1021/acs.chemmater.4c01557
Chem. Mater. 2024, 36, 10483−10495

deposit films by using common solution deposition techniques. The inks are analogous to the TiO_2 nanoparticle slurries used to form electrodes commonly employed in dye-sensitized and perovskite solar cells.[69] Here, we leverage either bar coating or spin coating to control the film thickness and morphology (Methods). Calcination at 500 °C in air burns off the ethylcellulose matrix and brings the α-V_2O_5 nanoparticles into intimate contact with one another to improve charge transport. Areas where ethylcellulose existed in the film are transformed into voids to yield a mesoporous film (Figure 6a). Calcination also oxidizes V_2O_5 with molecular oxygen to fill some oxygen vacancies that exist in as-deposited α-V_2O_5. $SnCl_2$ treatment resulted in the same color changes observed in the colloidal dispersions of bulk powders (Figure 1b) with increasing $SnCl_2$ concentration or treatment time, producing darker green films, which indicates that the chemistry is transferable to thin films (Figure 6b, top).

Electrical transport within the mesoporous vanadium oxide film was characterized in two-terminal planar devices. These devices comprise gold (Au) contacts, which were thermally evaporated onto the α-V_2O_5 film to form the source/drain electrodes. SEM images of the devices offer a closer examination of the mesoporous α-V_2O_5 film's microstructure within the active channel of the device (Figure 6b, bottom). Despite the high porosity of the film, the individual particles are sufficiently connected to allow for a percolation network between the source and drain electrodes (Figure 6c, inset). Current−voltage (I−V) characteristics of the two-terminal devices demonstrate that film conductivity (the slope of the I−V curve) is improved by increasing the $SnCl_2$ concentration (Figure 6c). The I−V characteristics of these Au/V_2O_5/Au devices exhibit nonlinear, symmetric behavior, expected for a metal/semiconductor/metal junction.

We further investigated the impact of $SnCl_2$ treatment on the electronic properties of V_2O_5 films through dark microwave conductivity and power reflection measurements. Dark microwave conductivity, a noncontact, high-frequency spectroscopic technique, probes the complex dielectric function of a thin film sample via modulation of the quality factor of a loaded ca. 10 GHz resonant cavity. Details on the analysis of the cavity resonance can be found in recent studies.[70] The cavity resonance for an untreated α-V_2O_5 nanoparticle film is both deeper and shifted to lower resonance frequency than that of the blank quartz substrate on which it was deposited (Figure 6d). The deeper resonance indicates that the untreated sample has appreciable 10 GHz conductance, most likely arising from the native concentration of oxygen vacancies and free electrons, whereas the bathochromic (red) shift of the resonance frequency arises primarily from the increased relative permittivity of α-V_2O_5. Increasing $SnCl_2$ treatment concentration induces a deepening and broadening of the cavity resonance, along with a further red shift of the resonance frequency, indicating an increase in both the dielectric constant and conductance of the film upon $SnCl_2$ treatment. These observations are consistent with an increase in the oxygen vacancy concentration and the incorporation of Sn^{4+} into the α-V_2O_5 crystal structure. For the α-V_2O_5 film treated with 0.1 M $SnCl_2$, the resonance frequency shows a slight blue shift compared to films treated with 0.05 and 0.01 M $SnCl_2$. We tentatively attribute this to variations in the thickness of the α-V_2O_5 layer with high concentrations of $SnCl_2$.

To quantify the changes in conductivity, we derived conductivity values from both microwave conductivity and electrical measurements (Figure 6e,f). These results reveal a clear trend of increasing conductivity with higher $SnCl_2$ concentrations, consistent with the rise in the free carrier concentrations inferred from the absorbance and EPR measurements discussed earlier. Notably, microwave conductivity (σ_M) increases by a factor of ca. 14 over the same concentration range of $SnCl_2$ treatments that produces a much smaller ca. 2−3-fold increase in two-terminal DC conductivity (σ_E) and a ca. 6-fold increase in four-terminal van der Pauw DC conductivity. This discrepancy arises from the different transport length scales probed by the two measurement techniques. Microwave conductivity can probe *local transport* occurring within the ca. 100 ps period of the 10 GHz probe (i.e., down to the single-particle level), whereas the DC conductivity measurement is only sensitive to long-range charge transport that occurs over a millimeter length scale through the percolated network of α-V_2O_5 particles and that is likely limited by transport across barriers between particles. It is this difference in the length scales probed by the techniques that results in a 10 GHz conductivity that is >10 times larger than that extracted using the DC conductivity techniques. It is important to note that the initial two-terminal DC measurements can often lead to inflated resistance values due to contributions from contact and lead resistances. In contrast, the van der Pauw method (a four-terminal DC measurement) minimizes errors caused by contact resistance and provides a more accurate reflection of the material's long-range electrical resistance.

The dark microwave conductivity and DC conductivity measurements both confirm that the topochemical transformation of V_2O_5 with $SnCl_2$ introduces conductive free electrons. The observed macroscopic device characteristics confirm that the optoelectronic changes induced by $SnCl_2$ are not confined to the isolated V_2O_5 nanoparticles, and long-range transport is possible through the mesoporous V_2O_5 film. The Fermi level, carrier density, and long-range conductivity can be finely tuned for solution-deposited mesoporous films of the V_2O_5 nanoparticles by low-temperature, solution-phase topochemical $SnCl_2$ reduction chemistry. The simultaneous achievement of good interparticle electronic communication and mesoporous film structure suggests that these films and devices could be good candidates for resistive switching devices based on, e.g., electrochemical random access memory (ECRAM) platforms.[71]

CONCLUSIONS

In summary, we demonstrated topochemical reduction of V^{5+} to V^{4+} and substitutional Sn^{4+} incorporation into α-V_2O_5 by utilizing a $SnCl_2$ solution at a low temperature of 65 °C. The redox process modifies the composition of α-V_2O_5 without changing the parent crystal structure and, by substitutional Sn^{4+} incorporation on the vanadium sublattice, affords a distinctive means of engineering oxygen vacancy and free electron concentrations without engendering transformations through a series of Wadsley phases. The $SnCl_2$ treatment is viable at room temperature and can be tuned using the $SnCl_2$ concentration and reaction time/temperature, which yield control over optoelectronic properties. Optical spectroscopy identified sub-band gap states associated with oxygen vacancies, and electron paramagnetic resonance spectroscopy and dark microwave conductivity measurement demonstrated an increase in free electrons because of the topochemical transformation. We showed that the $SnCl_2$ chemistry can also be applied to mesoporous α-V_2O_5 films fabricated via scalable solution

https://doi.org/10.1021/acs.chemmater.4c01557
Chem. Mater. 2024, 36, 10483−10495

deposition techniques. Electrical transport in the mesoporous films was probed with current−voltage analysis of two-terminal (four-terminal) devices and noncontact microwave conductivity measurements. Higher $SnCl_2$ concentrations led to a ca. 2.3-fold (6.1-fold) increase in conductivity in two-terminal (four-terminal) devices and ca. 14-fold increase in microwave conductivity measurements, indicating that our $SnCl_2$ chemistry may be applied to films, but the mesoporous network limits mobility. Our work serves as a valuable demonstration of tailoring the vanadium−oxygen system through post-synthetic top-down topochemical manipulation to impart electronic functionality as an alternative to bottom-up synthesis of exotic phases.

METHODS

Chemicals. 20 wt % α-V_2O_5 dispersed in acetone was purchased from US Research Nanomaterials, Inc. Anhydrous methanol, acetone, and DMSO were purchased from Sigma-Aldrich, transferred into a N_2-atmosphere glovebox, and stored over activated 3 Å molecular sieves. $SnCl_2$ was purchased from Sigma-Aldrich and used as received and stored in a N_2 glovebox. We note that handling nanomaterials poses health risks and vanadium oxides are often perceived to be carcinogenic, though they are used industrially for chemical synthesis; recent toxicology studies show that the carcinogenic nature of V_2O_5 requires further study.[72] Regardless, appropriate personal protective equipment should be used when handling these materials.

V_2O_5 Ink Preparation and Film Deposition. To fabricate the films for UV−vis−NIR absorption and dark microwave conductivity measurements, the α-V_2O_5 ink was deposited onto precut quartz substrates using either bar-coating or spin-coating methods in air. The Quartz/V_2O_5 sample underwent annealing in an oven for 30 min at 500 °C in ambient conditions. Optical profilometry measurements to determine the film thickness were performed on a Keyence VHX-7000 3D optical profilometer.

$SnCl_2$ Treatment. In the case of doped samples, α-V_2O_5 dispersed in acetone was weighed out in a vial of air. Acetone was evaporated from the sample on a hot plate and transferred as dry α-V_2O_5 powder to a N_2-atmosphere glovebox. $SnCl_2$ solution in methanol was added to the V_2O_5 powder at varying concentrations and for varying treatment times within the N_2-atmosphere glovebox. To remove unreacted $SnCl_2$ and any reaction byproducts, the V_2O_5 dispersion was centrifuged in the glovebox at 3000 rpm for 30 s, and the supernatant was poured off. Neat, dry methanol was added to the V_2O_5 nanoparticles and shaken up to redisperse. The process was repeated at least 3 times to observe minimal Cl 2p signal in XPS measurements. Mesoporous films were immersed in the same $SnCl_2$ solution. We avoided hydrolysis and oxidation side products by performing the $SnCl_2$ reduction chemistry in a N_2-atmosphere glovebox with solvents that are dry and stored over 3 Å molecular sieves.

Transmission Electron Microscopy. TEM samples were prepared by drop-casting a small amount of untreated and treated V_2O_5 samples onto carbon-coated Cu TEM grids. TEM imaging and diffraction data were collected on an FEI Tecnai F20 S/TEM operating at 200 kV. High-resolution scanning (S)TEM imaging and energy dispersive X-ray spectroscopy (EDX) were performed on a Thermo Fisher Scientific (TFS, formerly FEI) Spectra200 STEM operating at 200 kV with a convergence semiangle of 24.7 mrad and equipped with a TFS Super-X EDX detector.

X-ray Photoelectron Spectroscopy. V_2O_5 samples that were untreated and treated with $SnCl_2$ were drop-cast onto Au-coated glass substrates inside a N_2-atmosphere glovebox. Samples were transferred air-free from the glovebox to the XPS system through a load-lock. XPS data were obtained on a PHI Versa Probe III instrument using Al Kα radiation (1486.7 eV). The XPS data were calibrated with Au and/or Cu metal, which was cleaned via Ar-ion sputtering. The raw atomic concentration has a 5% error due to surface inhomogeneities, surface roughness, literature sensitivity values for peak integration, and so on.

Hard X-ray Photoelectron Spectroscopy (HAXPES). HAXPES was performed at the National Institute of Standards and Technology beamline SST-2 of National Synchrotron Light Source II at Brookhaven National Laboratory. The elemental core levels and valence bands were measured by using a 2 keV photon energy, 500 eV pass energy, and a 0.05 eV step size with the analyzer axis oriented in parallel with the photoelectron polarization vector. The valence bands of the materials were also measured using a 5 keV incident photon energy, 200 eV pass energy, and a 0.05 eV step size. The photon energies were selected using a double Si (111) crystal monochromator, and the beam energy was aligned to the Fermi level of a gold foil prior to measurement. Commercial equipment, instruments, or materials are identified in this study to adequately specify the experimental procedure. Such identification is not intended to imply recommendation or endorsement by the National Institute of Standards and Technology, nor is it intended to imply that the materials or equipment identified are necessarily the best available for the purpose.

X-ray Diffraction. XRD patterns were collected in air using a Bruker D8 Discover diffractometer with a GADDS four-circle detector (General Area Detector Diffraction System) and Cu Kα (1.5406 Å, 8.04 eV) radiation.

Raman Spectroscopy. Raman spectroscopy was performed on a Renishaw inVia system (Gloucestershire, U.K.) by using a 532 nm laser and 100× magnification or 50× long working distance objective lenses. The scattering light from the sample was directed by a grating with 1800 lines mm^{-1}.

Electron Paramagnetic Spin Resonance (EPR) Spectroscopy. V_2O_5 samples that were untreated and treated with $SnCl_2$ were prepared by adding V_2O_5 dispersions to a quartz (CFQ) 4 mm outer diameter tube. X-band (9.38 GHz) continuous-wave (CW) EPR measurements were performed on a Bruker ELEXSYS E500 spectrometer equipped with a super high-Q resonator, along with a cryogen-free temperature system (ColdEdge Technologies) and MercuryiTC temperature controller (Oxford Instruments) for low-temperature measurements. The Xepr software (Bruker) was used for data acquisition. Spectra were recorded at 60 K, using a modulation frequency of 100 kHz, a modulation amplitude of 10 G, and a microwave power of 0.1 mW.

UV−Visible−Near-Infrared Absorbance Spectroscopy. UV−vis−NIR absorbance measurements were performed on a Cary 5000 spectrophotometer equipped with a diffuse reflectance accessory with a photomultiplier tube and PbS detectors (DRA-2500). The sample was mounted at the center of the DRA-2500 integrating sphere, using a variable angle center mount holder, so that the measurement compensated for specular and diffuse reflectance/scattering from the sample. Baselines for 0 and 100% transmission were collected prior to measurement of the samples.

Dark Microwave Conductivity. Dark microwave conductivity measurements were performed in a custom-designed X-band copper microwave cavity, as described previously.[70] To calculate the conductance of each sample for the microwave measurement, we used the commercially available COMSOL Multiphysics (v4.3) finite element package to solve Maxwell's equations for the electromagnetic field distribution within the cavity, as described in detail elsewhere.[73] Replicates of each measurement were performed to obtain statistically meaningful average values and standard deviations.

V_2O_5 Device Fabrication. To fabricate the device, a commercially available glass substrate was used, followed by a cleaning process involving soap/DI water, acetone, and IPA. The α-V_2O_5 film was then deposited using the spin-coating method at 4000 rpm for 60 s, with a film thickness of approximately 2.6 μm (Figure S7). The glass/V_2O_5 film stack underwent annealing in an oven for 30 min at 500 °C under ambient conditions. Finally, a top metal contact (Au) was deposited using thermal deposition with a shadow mask, resulting in a thickness of 100 nm. The overall device configuration features six 0.1225 cm^2 device pixels on each substrate.

Electrical Transport Measurement. Electrical performance of our two-terminal devices was evaluated using a Keithley 4200 parameter analyzer by performing current−voltage (I−V) scans in ambient conditions at room temperature. The specified voltage bias

https://doi.org/10.1021/acs.chemmater.4c01557
Chem. Mater. 2024, 36, 10483−10495

(from the source electrode to the drain electrode) was applied to the device in the following sequence: −10 V → 0 V → 10 V. Four-terminal van der Pauw measurements were performed on samples prepared with dimensions of 1 cm × 1 cm. The measurements were performed using the M91 FastHall measurement controller in ambient conditions at room temperature, with a 1 T magnetic field applied and an excitation source current of 10 mA during the experiment.

Theory. We employed quasiparticle self-consistent GW (QSGW) approximation,[67] a many-body perturbative approach, which is a self-consistent form of Hedin's GW approximation.[74] Self-consistency eliminates the starting point dependence, and as a result, the discrepancies are much more systematic than conventional forms of GW.[75] Further, the excitonic correlations are included within a self-consistent extension of QSGW, called QSG$\hat{W}$,[76] where the electron−hole excitonic effects are taken into account by solving the Bethe−Salpeter equation in the presence of electron−hole ladder corrections. The QSG$\hat{W}$ is also fully self-consistent; the electronic eigenfunctions are recomputed in the presence of these excitonic correlations and vice versa, until self-energy, Green's functions, and optical polarizability, all of them achieve self-consistent convergence with desired accuracies. The importance of self-consistency in both QSGW and QSG$\hat{W}$ for different materials has been explored.[77] The theory and its application to a large number of both weakly and strongly correlated insulators is given in ref 76. To simulate the different kinds of vacancies, we prepared supercells of sizes 42, 56, and 84 atoms. The electronic and optical properties of the 56- and 84-atom supercells are very similar, and all qualitative conclusions for the two are same. We present the results for the 84-atom supercell in the present study.

■ ASSOCIATED CONTENT

Supporting Information

The Supporting Information is available free of charge at https://pubs.acs.org/doi/10.1021/acs.chemmater.4c01557.

Core-level hard X-ray photoelectron spectroscopy (HAXPES) for Sn^{4+} $3d_{3/2}$ and $3d_{5/2}$ and Cl 2p peaks; valence band HAXPES measured at 5 eV; electron diffraction patterns for untreated α-V_2O_5 and α-V_2O_5 treated with 0.05 M $SnCl_2$; Raman spectroscopy of V_2O_5 nanoparticles treated with different concentrations of $SnCl_2$; XRD diffraction patterns of V_2O_5 nanoparticles treated with different concentrations of $SnCl_2$ in acetone for 90 min; optical profilometry images of α-V_2O_5 films; stoichiometry from XPS derivation. (PDF)

■ AUTHOR INFORMATION

Corresponding Authors

Lance M. Wheeler − *National Renewable Energy Laboratory, Golden, Colorado 80401, United States;* orcid.org/0000-0002-1685-8242; Email: Lance.Wheeler@nrel.gov

Andrew J. Ferguson − *National Renewable Energy Laboratory, Golden, Colorado 80401, United States;* orcid.org/0000-0003-2544-1753; Email: Andrew.Ferguson@nrel.gov

Jeffrey L. Blackburn − *National Renewable Energy Laboratory, Golden, Colorado 80401, United States;* orcid.org/0000-0002-9237-5891; Email: Jeffrey.Blackburn@nrel.gov

Authors

Thanh Luan Phan − *National Renewable Energy Laboratory, Golden, Colorado 80401, United States;* orcid.org/0000-0002-2873-8176

Michelle A. Smeaton − *National Renewable Energy Laboratory, Golden, Colorado 80401, United States;* orcid.org/0000-0001-9114-1009

Swagata Acharya − *National Renewable Energy Laboratory, Golden, Colorado 80401, United States*

Shruti Hariyani − *Department of Chemistry, Texas A&M University, College Station, Texas 77843, United States*

Marlena E. Alexander − *National Renewable Energy Laboratory, Golden, Colorado 80401, United States*

Miranda I. Gonzalez − *National Renewable Energy Laboratory, Golden, Colorado 80401, United States*

Elisa M. Miller − *National Renewable Energy Laboratory, Golden, Colorado 80401, United States;* orcid.org/0000-0002-7648-5433

David W. Mulder − *National Renewable Energy Laboratory, Golden, Colorado 80401, United States;* orcid.org/0000-0003-0559-0145

Sarbajit Banerjee − *Department of Chemistry, Texas A&M University, College Station, Texas 77843, United States;* orcid.org/0000-0002-2028-4675

Katherine L. Jungjohann − *National Renewable Energy Laboratory, Golden, Colorado 80401, United States;* orcid.org/0000-0002-8132-1230

Complete contact information is available at: https://pubs.acs.org/10.1021/acs.chemmater.4c01557

Notes

The authors declare no competing financial interest.

■ ACKNOWLEDGMENTS

This work was authored, in part, by the National Renewable Energy Laboratory (NREL), operated by Alliance for Sustainable Energy, LLC, for the US Department of Energy (DOE) under Contract No. DE-AC36-08GO28308. The synthesis, thin film deposition, device fabrication, and material/device characterization (other than the EPR measurements) at NREL were supported as part of the Reconfigurable Materials Inspired by Nonlinear Neuron Dynamics (reMIND) Energy Frontier Research Center funded by the US Department of Energy (DOE), Office of Science, Basic Energy Sciences. The EPR measurements were performed as part of the "Controlling Spins + Interfaces: Low Power Electronics" Transformational Laboratory Directed Research and Development (LDRD) project, which is supported by the LDRD Program at NREL. S.A. is supported by the Computational Chemical Sciences program within the Office of Basic Energy Sciences, US Department of Energy under Contract No. DE-AC36-08GO28308. S.A. acknowledges insightful discussions with Mark van Schilfgaarde. S.A. acknowledges the use of the National Energy Research Scientific Computing Center (NERSC), under Contract No. DE-AC02-05CH11231 using NERSC award BES-ERCAP0021783, and the computational resources sponsored by the Department of Energy's Office of Energy Efficiency and Renewable Energy (the Kestrel HPC system) located at the National Renewable Energy Laboratory. The authors acknowledge Dr. Obadiah Reid for the development of the measurement and analysis routines used to collect and process the dark microwave conductivity data and for useful discussions of the 10 GHz complex permittivity. The authors acknowledge Nathan Balaich for optical profilometry measurements. The views expressed in the article do not necessarily represent the views of the DOE or the US Government. The US Government retains and the publisher, by accepting the article for publication, acknowledges that the US Government retains a nonexclusive, paid-up, irrevocable, worldwide license to publish or reproduce the published form of this work, or allow others to do so, for US Government purposes.

REFERENCES

(1) Bahlawane, N.; Lenoble, D. Vanadium Oxide Compounds: Structure, Properties, and Growth from the Gas Phase. *Chem. Vap. Deposition* **2014**, *20* (7−9), 299−311.

(2) Parija, A.; Waetzig, G. R.; Andrews, J. L.; Banerjee, S. Traversing Energy Landscapes Away from Equilibrium: Strategies for Accessing and Utilizing Metastable Phase Space. *J. Phys. Chem. C* **2018**, *122* (45), 25709−25728.

(3) Andrews, J. L.; Santos, D. A.; Meyyappan, M.; Williams, R. S.; Banerjee, S. Building Brain-Inspired Logic Circuits from Dynamically Switchable Transition-Metal Oxides. *Trends Chem.* **2019**, *1* (8), 711−726.

(4) Hu, P.; Hu, P.; Vu, T. D.; Li, M.; Wang, S.; Ke, Y.; Zeng, X.; Mai, L.; Long, Y. Vanadium Oxide: Phase Diagrams, Structures, Synthesis, and Applications. *Chem. Rev.* **2023**, *123* (8), 4353−4415.

(5) Fu, Q.; Zhao, H.; Sarapulova, A.; Dsoke, S. V_2O_5 as a Versatile Electrode Material for Postlithium Energy Storage Systems. *Appl. Res.* **2023**, *2* (3), No. 202200070.

(6) Zavalij, P. Y.; Whittingham, M. S. Structural Chemistry of Vanadium Oxides with Open Frameworks. *Acta Crystallogr., Sect. B* **1999**, *55* (5), 627−663.

(7) Slewa, L. H.; Abbas, T. A.; Ahmed, N. M. Effect of Sn Doping and Annealing on the Morphology, Structural, Optical, and Electrical Properties of 3D (Micro/Nano) V_2O_5 Sphere for High Sensitivity pH-EGFET Sensor. *Sens. Actuators, B* **2020**, *305*, No. 127515.

(8) Li, Z.; Zhang, C.; Liu, C.; Fu, H.; Nan, X.; Wang, K.; Li, X.; Ma, W.; Lu, X.; Cao, G. Enhanced Electrochemical Properties of Sn-Doped V_2O_5 as a Cathode Material for Lithium Ion Batteries. *Electrochim. Acta* **2016**, *222*, 1831−1838.

(9) Uma Shankar, V.; Govindarajan, G.; Gopalakrishnan, G.; Maiyalagan, M.; Salethraj, J. S. rGO-Encapsulated Sn-Doped V_2O_5 Nanorods for High-Performance Supercapacitors. *Mater. Today Commun.* **2021**, *27*, No. 102357.

(10) Rajeshwari, S.; Kumar, J. S.; Rajendrakumar, R. T.; Ponpandian, N.; Thangadurai, P. Influence of Sn Ion Doping on the Photocatalytic Performance of V_2O_5 Nanorods Prepared by Hydrothermal Method. *Mater. Res. Express* **2018**, *5* (2), No. 025507.

(11) Neelima, M.; Vandana, S.; Kathirvel, A.; Sivakumar, M.; Maheswari, A. U. Titanium Doped V_2O_5 Nanostructures by Chemical Synthesis for Photocatalytic Performance Enhancement. *Optik* **2022**, *252*, No. 168516.

(12) Jaya, T. P.; Jayaram, P.; Ramachandran, T.; Hajira, P.; Anumol, C. N.; Pradyumnan, P. P. Synthesis of Solid Solutions of Mn and Bi Substituted V_2O_5 and Substitutional Effect in Structural and Optoelectronic Behavior. *Physica B* **2012**, *407* (8), 1214−1218.

(13) Chen, M.; Liang, F.; Zou, Z.; Zhang, S.; Zhong, S.; Yu, F.; Jia, S.; Nong, J. Al-Doping Endows $V_2O_5{\cdot}4VO_2$ Enhanced Lithium Storage. *J. Alloys Compd.* **2024**, *983*, No. 173775.

(14) Haaß, F.; Adams, A. H.; Buhrmester, T.; Schimanke, G.; Martin, M.; Fuess, H. X-Ray Absorption and X-Ray Diffraction Studies on Molybdenum Doped Vanadium Pentoxide. *Phys. Chem. Chem. Phys.* **2003**, *5* (19), 4317−4324.

(15) Yu, D. M.; Zhang, S. T.; Liu, D. W.; Zhou, X. Y.; Xie, S. H.; Zhang, Q. F.; Liu, Y. Y.; Cao, G. Z. Effect of Manganese Doping on Li-Ion Intercalation Properties of V2O5 Films. *J. Mater. Chem.* **2010**, *20* (48), 10841−10846.

(16) Schofield, P.; Luo, Y.; Zhang, D.; Zaheer, W.; Santos, D.; Agbeworvi, G.; Ponis, J. D.; Handy, J. V.; Andrews, J. L.; Braham, E. J.; Balakrishna, A. R.; Banerjee, S. Doping-Induced Pre-Transformation to Extend Solid-Solution Regimes in Li-Ion Batteries. *ACS Energy Lett.* **2022**, *7* (10), 3286−3292.

(17) Keilholz, S.; Paul, R.; Dorsch, L. Y.; Kohlmann, H. In Situ X-Ray Diffraction Studies on the Reduction of V_2O_5 and WO_3 by Using Hydrogen. *Chem. − Eur. J.* **2023**, *29* (17), No. e202203932.

(18) Handy, J. V.; Zaheer, W.; Albers, R.; Agbeworvi, G.; Boyko, T. D.; Bakhmoutov, V.; Bhuvanesh, N.; Banerjee, S. Protecting Groups in Insertion Chemistry: Site-Selective Positioning of Lithium Ions in Intercalation Hosts. *Matter* **2023**, *6* (4), 1125−1139.

(19) Agbeworvi, G.; Zaheer, W.; Handy, J. V.; Andrews, J. L.; Perez-Beltran, S.; Jaye, C.; Weiland, C.; Fischer, D. A.; Balbuena, P. B.; Banerjee, S. Toggling Stereochemical Activity through Interstitial Positioning of Cations between 2D V_2O_5 Double Layers. *Chem. Mater.* **2023**, *35* (17), 7175−7188.

(20) Meng, Z.; Yan, H.; Qin, P.; Zhou, X.; Wang, X.; Chen, H.; Liu, L.; Liu, Z. Topotactic Transition: A Promising Opportunity for Creating New Oxides. *Adv. Funct. Mater.* **2023**, *33* (46), No. 2305225.

(21) Luo, Y.; Handy, J. V.; Das, T.; Ponis, J. D.; Albers, R.; Chiang, Y.-H.; Pharr, M.; Schultz, B. J.; Gobbato, L.; Brown, D. C.; Chakraborty, S.; Banerjee, S. Effect of Pre-Intercalation on Li-Ion Diffusion Mapped by Topochemical Single-Crystal Transformation and Operando Investigation. *Nat. Mater.* **2024**, *23*, 960−968.

(22) Orvis, T.; Surendran, M.; Liu, Y.; Niu, S.; Muramoto, S.; Grutter, A. J.; Ravichandran, J. Electron Doping $BaZrO_3$ via Topochemical Reduction. *ACS Appl. Mater. Interfaces* **2019**, *11* (24), 21720−21726.

(23) Liang, Z.; Amano Patino, M.; Hendrickx, M.; Hadermann, J.; Hayward, M. A. Microstructural Activation of a Topochemical Reduction Reaction. *ACS Org. Inorg. Au* **2022**, *2* (1), 75−82.

(24) Takamatsu, T.; Kato, M.; Noji, T.; Koike, Y. Low-Temperature Synthesis of the Infinite-Layer Compound $LaNiO_2$ by Soft-Chemical Techniques. *Jpn. J. Appl. Phys.* **2010**, *49* (9R), No. 093101.

(25) Ikeda, A.; Krockenberger, Y.; Irie, H.; Naito, M.; Yamamoto, H. Direct Observation of Infinite NiO2 Planes in $LaNiO_2$ Films. *Appl. Phys. Express* **2016**, *9* (6), No. 061101.

(26) Dixon, E.; Hadermann, J.; Hayward, M. A. Structures and Magnetism of $La_{1-x}Sr_xMnO_{3-(0.5+x)/2}$ ($0.67 \leq x \leq 1$) Phases. *Chem. Mater.* **2012**, *24* (8), 1486−1495.

(27) Kitchen, H. J.; Saratovsky, I.; Hayward, M. A. Topotactic Reduction as a Synthetic Route for the Preparation of Low-Dimensional Mn(II) Oxide Phases: The Structure and Magnetism of $LaAMnO_{4-x}$ (A = Sr, Ba). *Dalton Trans.* **2010**, *39* (26), 6098−6105.

(28) Denis Romero, F.; Burr, S. J.; McGrady, J. E.; Gianolio, D.; Cibin, G.; Hayward, M. A. $SrFe_{0.5}Ru_{0.5}O_2$: Square-Planar Ru^{2+} in an Extended Oxide. *J. Am. Chem. Soc.* **2013**, *135* (5), 1838−1844.

(29) Tassel, C.; Seinberg, L.; Hayashi, N.; Ganesanpotti, S.; Ajiro, Y.; Kobayashi, Y.; Kageyama, H. Sr_2FeO_3 with Stacked Infinite Chains of FeO_4 Square Planes. *Inorg. Chem.* **2013**, *52* (10), 6096−6102.

(30) Yajima, T.; Kitada, A.; Kobayashi, Y.; Sakaguchi, T.; Bouilly, G.; Kasahara, S.; Terashima, T.; Takano, M.; Kageyama, H. Epitaxial Thin Films of $ATiO_{3-x}H_x$ (A = Ba, Sr, Ca) with Metallic Conductivity. *J. Am. Chem. Soc.* **2012**, *134* (21), 8782−8785.

(31) Kobayashi, Y.; Hernandez, O. J.; Sakaguchi, T.; Yajima, T.; Roisnel, T.; Tsujimoto, Y.; Morita, M.; Noda, Y.; Mogami, Y.; Kitada, A.; Ohkura, M.; Hosokawa, S.; Li, Z.; Hayashi, K.; Kusano, Y.; Kim, J.; Tsuji, N.; Fujiwara, A.; Matsushita, Y.; Yoshimura, K.; Takegoshi, K.; Inoue, M.; Takano, M.; Kageyama, H. An Oxyhydride of $BaTiO_3$ Exhibiting Hydride Exchange and Electronic Conductivity. *Nat. Mater.* **2012**, *11* (6), 507−511.

(32) Enjalbert, R.; Galy, J. A Refinement of the Structure of V_2O_5. *Acta Crystallogr., Sect. C* **1986**, *42* (11), 1467−1469.

(33) Correal, S.; Hernández-Gómez, D.; Esquivel, A. S.; Cardona-Rodríguez, A.; Reiber, A.; Hernandez, Y.; González-Hernández, R.; Ramírez, J. G. Tuning Electronic and Magnetic Properties through Disorder in V_2O_5 Nanoparticles. *Sci. Rep.* **2023**, *13* (1), No. 6752.

(34) McColl, K.; Johnson, I.; Corà, F. Thermodynamics and Defect Chemistry of Substitutional and Interstitial Cation Doping in Layered α-V_2O_5. *Phys. Chem. Chem. Phys.* **2018**, *20* (22), 15002−15006.

(35) Pozdnyakova, O.; Megyeri, J.; Kuzmann, E.; Szirtes, L. X-Ray Powder Diffraction Study of Chromium-Vanadium Oxide Compounds Prepared by "Soft Chemistry" Methods. *Open Chem.* **2006**, *4* (4), 760−772.

(36) Reed, B. W.; Huynh, V.; Tran, C.; Koski, K. J. Brillouin Scattering of V_2O_5 and Sn-Intercalated V_2O_5. *Phys. Rev. B* **2020**, *102* (5), No. 054109.

(37) Wang, M.; Koski, K. J. Reversible Chemochromic MoO_3 Nanoribbons through Zerovalent Metal Intercalation. *ACS Nano* **2015**, *9* (3), 3226−3233.

https://doi.org/10.1021/acs.chemmater.4c01557
Chem. Mater. 2024, 36, 10483−10495

(38) Koski, K. J.; Wessells, C. D.; Reed, B. W.; Cha, J. J.; Kong, D.; Cui, Y. Chemical Intercalation of Zerovalent Metals into 2D Layered Bi_2Se_3 Nanoribbons. *J. Am. Chem. Soc.* **2012**, *134* (33), 13773−13779.
(39) Wang, M.; Williams, D.; Lahti, G.; Teshima, S.; Aguilar, D. D.; Perry, R.; Koski, K. J. Chemical Intercalation of Heavy Metal, Semimetal, and Semiconductor Atoms into 2D Layered Chalcogenides. *2D Mater.* **2018**, *5* (4), No. 045005.
(40) Lu, Q.; Bishop, S. R.; Lee, D.; Lee, S.; Bluhm, H.; Tuller, H. L.; Lee, H. N.; Yildiz, B. Electrochemically Triggered Metal−Insulator Transition between VO_2 and V_2O_5. *Adv. Funct. Mater.* **2018**, *28* (34), No. 1803024.
(41) Papoutsakis, D.; Ichimura, A.; Young, J.; Jackson, J.; Nocera, D. Structural and Magnetic Properties of Vanadyl Dichloride Solvates: From Molecular Units to Extended Hydrogen-Bonded Solids. *Dalton Trans.* **2004**, *0* (2), 224−228.
(42) Ewings, P. F. R.; Harrison, P. G. Derivatives of Bivalent Germanium, Tin and Lead. Part XVII. Some Oxidative Addition Reactions of Tin(II) Halides. *Inorg. Chim. Acta* **1976**, *18*, 165−172.
(43) Messin, G.; Janier-Dubry, J. L. On the Oxidation of Tin (II) Salts with Oxygen or Chlorine. *Inorg. Nucl. Chem. Lett.* **1979**, *15* (11), 409−412.
(44) Wang, Q.; Brier, M.; Joshi, S.; Puntambekar, A.; Chakrapani, V. Defect-Induced Burstein-Moss Shift in Reduced V_2O_5 Nanostructures. *Phys. Rev. B* **2016**, *94* (24), No. 245305.
(45) Scanlon, D. O.; Walsh, A.; Morgan, B. J.; Watson, G. W. An Ab Initio Study of Reduction of V_2O_5 through the Formation of Oxygen Vacancies and Li Intercalation. *J. Phys. Chem. C* **2008**, *112* (26), 9903−9911.
(46) Suthirakun, S.; Jungthawan, S.; Limpijumnong, S. Effect of Sn-Doping on Behavior of Li-Intercalation in V_2O_5 Cathode Materials of Li-Ion Batteries: A Computational Perspective. *J. Phys. Chem. C* **2018**, *122* (11), 5896−5907.
(47) Themlin, J.-M.; Chtaïb, M.; Henrard, L.; Lambin, P.; Darville, J.; Gilles, J.-M. Characterization of Tin Oxides by X-Ray-Photoemission Spectroscopy. *Phys. Rev. B* **1992**, *46* (4), 2460−2466.
(48) Lin, A. W. C.; Armstrong, N. R.; Kuwana, T. X-Ray Photoelectron/Auger Electron Spectroscopic Studies of Tin and Indium Metal Foils and Oxides. *Anal. Chem.* **1977**, *49* (8), 1228−1235.
(49) Hryha, E.; Rutqvist, E.; Nyborg, L. Stoichiometric Vanadium Oxides Studied by XPS. *Surf. Interface Anal.* **2012**, *44* (8), 1022−1025.
(50) Wu, Q.-H.; Thissen, A.; Jaegermann, W.; Liu, M. Photoelectron Spectroscopy Study of Oxygen Vacancy on Vanadium Oxides Surface. *Appl. Surf. Sci.* **2004**, *236* (1), 473−478.
(51) Siol, S.; Mann, J.; Newman, J.; Miyayama, T.; Watanabe, K.; Schmutz, P.; Cancellieri, C.; Jeurgens, L. P. H. Concepts for Chemical State Analysis at Constant Probing Depth by Lab-Based XPS/HAXPES Combining Soft and Hard X-Ray Sources. *Surf. Interface Anal.* **2020**, *52* (12), 802−810.
(52) Walsh, A.; Payne, D. J.; Egdell, R. G.; Watson, G. W. Stereochemistry of Post-Transition Metal Oxides: Revision of the Classical Lone Pair Model. *Chem. Soc. Rev.* **2011**, *40* (9), 4455−4463.
(53) Razek, S. A.; Popeil, M. R.; Wangoh, L.; Rana, J.; Suwandaratne, N.; Andrews, J. L.; Watson, D. F.; Banerjee, S.; Piper, L. F. J. Designing Catalysts for Water Splitting Based on Electronic Structure Considerations. *Electron. Struct.* **2020**, *2* (2), No. 023001.
(54) Bachmann, H. G. The Crystal Structure of Vanadium Pentoxide. *Z. Kristallogr.* **1961**, *115* (1−2), 110−131, DOI: 10.1524/zkri.1961.115.1-2.110.
(55) Kim, H.-S.; Cook, J. B.; Lin, H.; Ko, J. S.; Tolbert, S. H.; Ozolins, V.; Dunn, B. Oxygen Vacancies Enhance Pseudocapacitive Charge Storage Properties of MoO_{3-x}. *Nat. Mater.* **2017**, *16* (4), 454−460.
(56) Yoshikawa, A.; Yagisawa, K.; Shimoda, M. Crystal Structure and Hydrogen Occupation in HxV2O5(X = 0.0−3.9). *J. Mater. Sci.* **1994**, *29* (5), 1319−1323.
(57) Mil'vidsky, M. G.; Osvensky, V. B.; Shifrin, S. S. Effect of Doping on Formation of Dislocation Structure in Semiconductor Crystals. *J. Cryst. Growth* **1981**, *52*, 396−403.
(58) Satto, C.; Sciau, P.; Dooryhee, E.; Galy, J.; Millet, P. The $\delta \rightarrow \varepsilon \rightarrow \gamma$ LiV_2O_5 "High Temperature" Phase Transitions Evidenced by Synchrotron X-Ray Powder Diffraction Analysis. *J. Solid State Chem.* **1999**, *146* (1), 103−109.
(59) Onoda, M.; Kagami, T. Crystal Structures and Electronic Properties in the Crossover Region between the Spin-Gap System CaV_2O_5 and the Linear-Chain System NaV_2O_5. *J. Phys.: Condens. Matter* **1999**, *11* (17), 3475.
(60) Onoda, M.; Nishiguchi, N. LETTER TO THE EDITOR: Crystal Structure and Spin Gap State of CaV_2O_5. *J. Solid State Chem.* **1996**, *127* (2), 359−362.
(61) Grégoire, G.; Baffier, N.; Kahn-harari, A.; Badot, J. X-Ray Powder Diffraction Study of a New Vanadium Oxide $Cr_{0.11}V_2O_{5.16}$ Synthesized by a Sol−Gel Process. *J. Mater. Chem.* **1998**, *8* (9), 2103−2108.
(62) Shannon, R. D. Revised Effective Ionic Radii and Systematic Studies of Interatomic Distances in Halides and Chalcogenides. *Acta Crystallogr., Sect. A* **1976**, *32* (5), 751−767.
(63) Sidey, V. On the Effective Ionic Radii for the Tin(II) Cation. *J. Phys. Chem. Solids* **2022**, *171*, No. 110992.
(64) Yaseen, M. W.; P Maman, M.; Mishra, S.; Mohammad, I.; Li, X. Strategies to Alleviate Distortive Phase Transformations in Li-Ion Intercalation Reactions: An Example with Vanadium Pentoxide. *Nanoscale* **2024**, *16* (20), 9710−9727.
(65) Luca, V.; MacLachlan, D. J.; Bramley, R. Electron Paramagnetic Resonance and Electron Spin Echo Study of Supported and Unsupported Vanadium Oxides. *Phys. Chem. Chem. Phys.* **1999**, *1* (10), 2597−2606.
(66) Vanhaelst, M.; Clauws, P. EPR Spectrum of the Oxygen Vacancy in Single Crystals V2O5. *Phys. Status Solidi B* **1978**, *87* (2), 719−723.
(67) van Schilfgaarde, M.; Kotani, T.; Faleev, S. Quasiparticle Self-Consistent GW Theory. *Phys. Rev. Lett.* **2006**, *96* (22), No. 226402.
(68) Garcia, C.; Radha, S. K.; Acharya, S.; Lambrecht, W. R. L. Quasiparticle Band Structure and Excitonic Optical Response in V_2O_5 Bulk and Monolayer. *Phys. Rev. B* **2024**, *110* (8), No. 085102.
(69) Todinova, A.; Idígoras, J.; Salado, M.; Kazim, S.; Anta, J. A. Universal Features of Electron Dynamics in Solar Cells with TiO_2 Contact: From Dye Solar Cells to Perovskite Solar Cells. *J. Phys. Chem. Lett.* **2015**, *6* (19), 3923−3930.
(70) Reid, O. G.; Moore, D. T.; Li, Z.; Zhao, D.; Yan, Y.; Zhu, K.; Rumbles, G. Quantitative Analysis of Time-Resolved Microwave Conductivity Data. *J. Phys. D: Appl. Phys.* **2017**, *50* (49), No. 493002.
(71) Talin, A. A.; Li, Y.; Robinson, D. A.; Fuller, E. J.; Kumar, S. ECRAM Materials, Devices, Circuits and Architectures: A Perspective. *Adv. Mater.* **2023**, *35* (37), No. 2204771.
(72) MacGregor, J. A.; White, D. J.; Williams, A. L. The Limitations of Using the NTP Chronic Bioassay on Vanadium Pentoxide in Risk Assessments. *Regul. Toxicol. Pharmacol.* **2020**, *113*, No. 104650.
(73) Ferguson, A. J.; Reid, O. G.; Nanayakkara, S. U.; Ihly, R.; Blackburn, J. L. Efficiency of Charge-Transfer Doping in Organic Semiconductors Probed with Quantitative Microwave and Direct-Current Conductance. *J. Phys. Chem. Lett.* **2018**, *9* (23), 6864−6870.
(74) Hedin, L. New Method for Calculating the One-Particle Green's Function with Application to the Electron-Gas Problem. *Phys. Rev.* **1965**, *139* (3A), A796−A823.
(75) Pashov, D.; Acharya, S.; Lambrecht, W. R. L.; Jackson, J.; Belashchenko, K. D.; Chantis, A.; Jamet, F.; van Schilfgaarde, M. Questaal: A Package of Electronic Structure Methods Based on the Linear Muffin-Tin Orbital Technique. *Comput. Phys. Commun.* **2020**, *249*, No. 107065.
(76) Cunningham, B.; Grüning, M.; Pashov, D.; van Schilfgaarde, M. QSGŴ: Quasiparticle Self-Consistent GW with Ladder Diagrams in W. *Phys. Rev. B* **2023**, *108* (16), No. 165104.
(77) Acharya, S.; Pashov, D.; Rudenko, A. N.; Rösner, M.; van Schilfgaarde, M.; Katsnelson, M. I. Importance of Charge Self-Consistency in First-Principles Description of Strongly Correlated Systems. *npj Comput. Mater.* **2021**, *7* (1), 208.